crystals

MDPI

Article

Comparison of Durability and Gamma-Ray Shielding Performance of High-Velocity Oxygen Fuel Tungsten Carbide-Based Coatings on Cold-Rolled Steel Surface

Yeong-Ho Son, Seung Heon Baek, Beom Kyu Kim, Jeong Ho Hwang, Jae Hun Lee and Geun Dong Song *

FNC Technology Co., Ltd., 32 Fl., 13 Heungdeok 1-ro, Giheung-gu, Yongin-si 16954, Republic of Korea
* Correspondence: gdsong@fnctech.com; Tel.: +82-31-8005-5977

Abstract: This paper provides a comparative evaluation of the mechanical properties, corrosion resistance, and gamma-ray shielding performance of four different types of tungsten carbide (WC)-NiCr coatings deposited on cold-rolled steel surfaces, which are used as materials for low- and intermediate-level radioactive waste (LILW) storage containers. The four types of coatings were classified as WC-85, WC-73, WC-66, and WC-39 according to their WC content and were applied to the cold-rolled steel surfaces using the High-Velocity Oxygen Fuel (HVOF) spraying process. The performance of the layered coatings was analyzed in terms of their microstructure, hardness, wear resistance, adhesion strength, corrosion properties, and gamma-ray shielding characteristics. Coatings with elevated WC contents showed enhanced mechanical properties and gamma-ray shielding effectiveness, whereas coatings with relatively lower WC contents and higher NiCr contents exhibited greater corrosion resistance. This paper discusses the performance of WC-NiCr coatings from the viewpoint of enhancing the durability and safety of commercial LILW storage containers.

Keywords: HVOF; tungsten carbide coatings; mechanical properties; corrosion resistance; gamma-ray shielding; radioactive waste storage container

check for updates

Academic Editor: José L. García

Received: 20 November 2024
Revised: 11 December 2024
Accepted: 19 December 2024
Published: 27 December 2024

Citation: Son, Y.-H.; Baek, S.H.; Kim, B.K.; Hwang, J.H.; Lee, J.H.; Song, G.D. Comparison of Durability and Gamma-Ray Shielding Performance of High-Velocity Oxygen Fuel Tungsten Carbide-Based Coatings on Cold-Rolled Steel Surface. *Crystals* **2025**, *15*, 21. https://doi.org/10.3390/cryst15010021

Copyright: © 2024 by the authors. Licensee MDPI, Basel, Switzerland. This article is an open access article distributed under the terms and conditions of the Creative Commons Attribution (CC BY) license (https://creativecommons.org/licenses/by/4.0/).

1. Introduction

The safe management and disposal of radioactive waste is a critical challenge for the sustainable development of the nuclear industry. LILWs are particularly significant due to their large volume and the complexities involved in their treatment and disposal, necessitating long-term storage and robust management. For the storage of such waste, containers with enhanced durability and effective radiation shielding performance are essential to minimize environmental and human health risks [1,2].

Conventional storage containers, predominantly 200 L or 320 L steel drums, are typically made of cold-rolled steel and designed for temporary storage in surface or near-surface facilities before disposal. The specific performance requirements for these containers, such as shielding efficiency and long-term durability, are determined based on the disposal strategies of each country. However, such containers often face issues such as corrosion, wear, and degradation over time. These problems are primarily caused by surface treatments like painting, which initially provide protection but degrade over time due to mechanical impacts during handling and environmental exposure, leading to delamination, cracking, and compromised corrosion resistance [3–5]. Additionally, these containers typically lack inherent shielding capabilities, making them unsuitable for the long-term storage of radioactive waste.

To address these challenges, extensive research has focused on coating-based technologies aimed at enhancing container durability. Polymer-based coatings have been explored for their initial corrosion resistance and ease of application [6–9]. However, organic coatings, such as polymers, suffer from significant degradation during long-term storage, including thermal instability and chemical decomposition, ultimately compromising their protective capabilities.

Ceramic–metal composite coatings have shown great potential as a durable solution for storage containers. For instance, WC-Co coatings significantly improve wear resistance and extend the lifespan of structural components [10–12]. Similarly, Cr_3C_2-NiCr coatings exhibit enhanced tribological performance, particularly in abrasive environments [13,14]. Additionally, ceramic–metal composite coatings have been extensively studied for their corrosion resistance. Cr-rich WC-based cermet coatings applied via HVOF have demonstrated significant enhancements in oxidation and corrosion resistance, particularly on 316L stainless steel under high-temperature conditions [15]. Furthermore, Cr has been shown to improve the corrosion resistance of WC-Ni-based composites, while the incorporation of Mo into these composites has further enhanced their performance in challenging environments [16]. Cr_3C_2-NiCr coatings have also exhibited remarkable long-term corrosion resistance in 3.5 wt.% NaCl solutions, particularly in the presence of sulfides, compared to uncoated Q345 steel. This improvement was attributed to the formation of a dense protective film and the accumulation of corrosion products on the coating surface after 70 days of immersion [17]. Ceramic–metal composite coatings are also widely applied in industries such as power generation and aerospace, where they contribute to the durability and corrosion resistance of structural components under demanding operational conditions [18–20].

Several application methods exist for ceramic–metal composites, with HVOF spraying being widely recognized for its ability to produce coatings with strong bonding strength, dense microstructures, and superior mechanical properties [20–23]. WC-based coatings, frequently utilized in HVOF processes, are particularly notable for their exceptional hardness and wear resistance, effectively minimizing surface damage and ensuring long-term stability [24–27]. Furthermore, WC-based coatings containing tungsten are expected to exhibit superior gamma-ray shielding performance, a critical requirement for radioactive waste storage. Compared to conventional storage containers, which typically lack inherent shielding capabilities, the high atomic number of tungsten significantly enhances the probability of photoelectric absorption, while its high density improves gamma-ray attenuation through Compton scattering and pair production interactions [28]. These attributes suggest that WC-based coatings could provide a substantial improvement in shielding performance over traditional cold-rolled steel containers.

While these findings have been widely applied in various industries, their application to radioactive waste storage containers remains unexplored. Therefore, this study focuses on evaluating and comparing coatings with varying WC contents to identify suitable materials for enhancing the durability and radiation shielding performance of storage containers. The evaluation includes key mechanical properties such as adhesion strength, hardness, and wear resistance, alongside corrosion resistance and gamma-ray shielding performance. The results aim to provide a practical solution for the safe and long-term management of radioactive waste.

2. Materials and Methods

2.1. Materials and Coating Procedure

An ASTM A1008 CS Type B cold-rolled steel plate (C—0.0026, P—0.0102, S—0.0045, Mn—0.092, Si—0.001, Fe—balance in wt.%) was used as the substrate material in this

study. For coating deposition, an A1008 CS Type B plate was machined to dimensions of 100 mm × 100 mm × 1.2 mm. To examine the effect of WC content on coating performance, four commercially available powders with varying WC contents were selected as coating materials. The chemical compositions of these powders are listed in Table 1, and the samples were labeled WC-85, WC-73, WC-66, and WC-39 according to their respective WC content.

Table 1. The chemical composition and particle size of powder materials for HVOF coating.

Sample	Chemical Composition (wt.%)					Particle Size (μm)
	W	C	Ni	Cr	Co	
WC-85	79.2	5.4	10.2	5.2	-	15–45
WC-73	66.7	5.9	7.4	19.9	0.1	16–46
WC-66	59.5	6.4	16.3	17.7	-	10–53
WC-39	35.3	3.6	18.1	43.0	-	16–45

The HVOF technique was chosen due to its capability to produce dense, high-bond-strength coatings with minimal porosity, a characteristic essential for applications demanding durability and enhanced corrosion resistance [22]. The particle size distribution of the powders, ranging between 10 μm and 60 μm, was determined and optimized by the manufacturer to minimize porosity and defects during the HVOF coating process. The specific particle size ranges selected for each powder are detailed in Table 1. This optimized range ensures optimal flowability and deposition characteristics for high-quality coatings [29].

The coatings used in this study were sourced from a manufacturer who optimized both the powder compositions and HVOF process parameters to ensure high coating quality. The specific parameters, as detailed in Table 2, were provided by the manufacturer as part of the optimized process.

Table 2. Parameters for HVOF coating process.

Operation Process	Parameter	Value
Spray Equipment Supplements	Gun Type	JK 3000
	Nozzle (Anode) (cm)	0.64 × 22.86
	Electrode (Cathode)	N/A
	Type of Gas (Primary)	Oxygen
	Type of Gas (Secondary)	Hydrogen
Powder Feeder	Powder Gas Type	Argon
	Carrier Gas (kPa)	1034 ± 34
	Carrier Gas (FMR)	9 ± 1
	Feed Rate (g/min)	25 ± 5
	Feeder Hose to Gun, Inner Dia. (cm).	0.47
	Feeder Hose to Gun, Length (m)	3~5
Coating Data	Pre-heat method	1 cycle of flame
	Gun-to-Work Distance (cm)	22.86 ± 1.27
	Applicable Angle	90 ± 5°
	Gun Traverse Speed (mm/s)	5
	Surface Speed (ft/min) (ref.)	188 ± 18
Cooling Substrate	Auxiliary Cooling Gas Pressure (kPa)	275 (Min.)
	Auxiliary Cooling Gas Distance (cm)	7.6~17.8
	Auxiliary Cooling Gas Angle	45° (Min.)

Prior to coating, the substrates were pre-cleaned in acetone for 5 min to remove surface contaminants and then blast-cleaned with aluminum oxide abrasive media (particle size:

250–400 μm) for an additional 5 min to improve coating adhesion. Each WC-containing powder was deposited onto the substrates using JK3000 HVOF equipment. To achieve the target coating thickness of approximately 250 μm, the deposition was performed with an average of 70 single passes (35 round trips) per sample, with minor variations depending on the powder characteristics. To ensure uniformity, the same parameter set was consistently applied across all samples.

2.2. Microstructural and Mechanical Characterization

After the coating process, the cross-section of each sample was observed and analyzed using SEM (CLARA, TESCAN, Brno, Czech Republic) and EDS (Ultim Max, OXFORD, Abingdon, UK) to characterize the microstructural features. To avoid damage to and the distortion of the coating cross-section, the sample cross-sections were pretreated using an ion beam milling system prior to SEM analysis.

The mechanical properties of the coating were evaluated through hardness, wear resistance, and bonding strength tests. Vickers hardness tests (Wilson VH-3300, BUEHLER, Lake Bluff, IL, USA) were conducted on the cross-section of each sample in accordance with ASTM E384 [30]. Indentations were made with a load of 300 gf for 10 s, with measurements performed five times per sample to ensure reproducibility. In addition, the distance between indentations was maintained at 0.3 mm to minimize the effect of nearby indentations [31].

The wear properties of the coating samples were evaluated using the Taber abrasion test in accordance with ASTM F1978 [32]. Previous studies on the effects of abrasive wheels under a maximum load of 10 N have shown that the H-10 (d_{50} = 75 μm, SiC, Al_2O_3-based ceramic binder) and S-35 (sintered hard metal, 1626 ± 35 HV30, inclined notches) wheels do not produce sufficient wear in HVOF WC-based coatings. In contrast, the H-22 abrasive wheel (d_{50} = 165 μm, SiC, Al_2O_3-based ceramic binder) generates adequate wear, making it suitable for evaluating the wear characteristics of high-hardness WC-based coatings [22,33]. Consequently, in this study, all tests were performed using the H-22 wheel to ensure sufficient wear on the coating samples. The specimen for the Taber abrasion test was machined into the shape shown in Figure 1a. Testing was conducted at room temperature (25 °C) and a humidity level of 30–65% using the Taber abrasion tester (QM600T, QMESYS, Uiwang-si, Republic of Korea) shown in Figure 1b, with an applied maximum load of 500 g on the abrasive wheel. The coatings were tested for up to 30,000 cycles, after which the thickness reduction in each sample was measured using a digital micrometer to compare wear resistance.

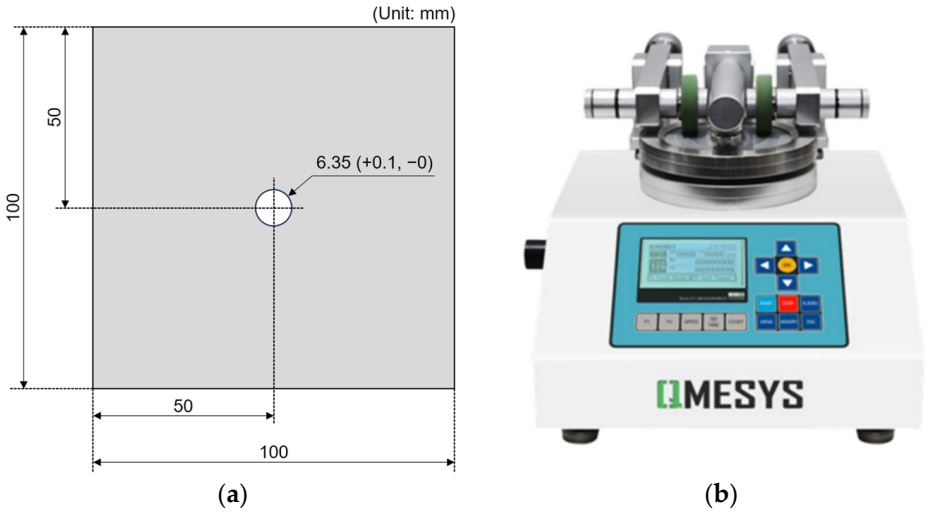


Figure 1. Taber abrasion test specimen (**a**) and testing apparatus (**b**).

The adhesion strength of the coating was evaluated using a universal tensile testing machine in accordance with ASTM C633 [34]. Machined coupons were prepared, and custom jigs were fabricated to secure the specimen in the saddle and holder, ensuring compatibility with the testing machine, as shown in Figure 2. The specimens (diameter: 25.4 mm) were cleaned with ethanol to remove impurities from the coating and substrate surfaces. FM-1000 adhesive was then used to bond the specimen to the jig, and the assembly was cured in an oven at 180 °C for 5 h to enhance bonding strength. After curing, the specimen was mounted vertically in the tensile testing machine with proper alignment in the saddle and holder, and a small preload was applied to ensure stable positioning in the grippers. Testing was conducted by applying a tensile load at a constant crosshead speed of 0.0167 mm/s until failure, and the maximum load recorded at failure was noted as the coating's adhesion strength. To ensure reproducibility, the test was repeated five times under identical conditions.

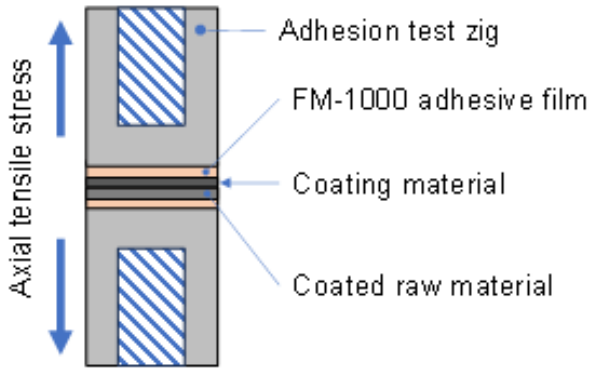


Figure 2. Adhesion test specimen setup with adhesion test jig, FM-1000 adhesive, coating sample.

2.3. Electrochemical Corrosion Test

To perform the electrochemical test, the as-coated sample was machined into a circular shape (diameter: 16.9 mm, thickness: 1.2 mm) as shown in Figure 3. The test solution used in this study was an oxygen-saturated aqueous solution adjusted to pH 5.0 with sulfuric acid. This solution was prepared to simulate the condensate that forms on the surface of LILW storage containers under storage conditions, as well as the effects of acidic rain [35].

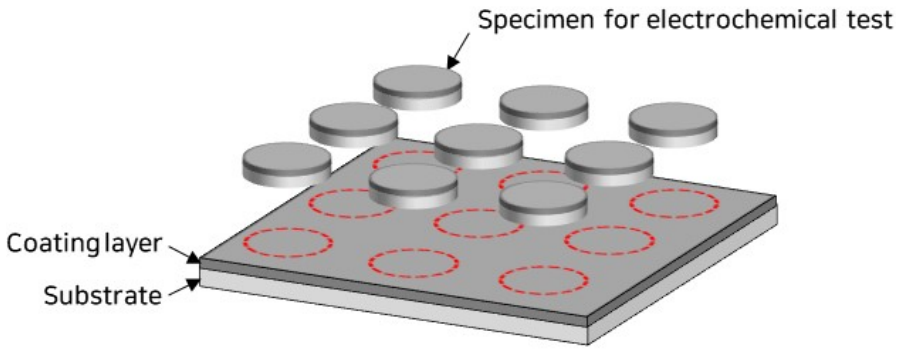
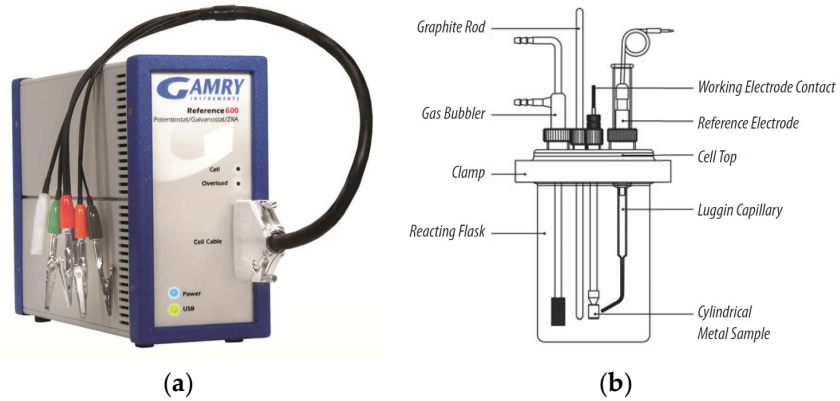


Figure 3. Schematic for the preparation of specimens for electrochemical tests.

To evaluate the corrosion current density (i_{corr}), potentiodynamic polarization tests were conducted with a potentiostat (Reference 600, GAMRY, Louis Drive, Warminster, PA, USA) and a three-electrode cell setup, as shown in Figure 4. A saturated calomel electrode (SCE) and platinum wire served as the reference and counter electrodes, respectively. After the open circuit potential (OCP) was stabilized, polarization scans for each specimen were initiated either 10 mV below the OCP in the anodic direction or 10 mV above the OCP in the

cathodic direction. The scan rate was set to 1 mV/s. The anodic and cathodic polarization curves were then combined into a single graph [36]. The i_{corr} for each coating sample were calculated by using the Tafel extrapolation method, based on cathodic polarization curves. In addition, the reproducibility of the polarization curve was verified by repeating the tests with freshly prepared electrodes and test solutions.



(**a**) (**b**)

Figure 4. Test apparatus for the electrochemical test: (**a**) Potentiostat and (**b**) three-electrode cell.

2.4. Gamma-Ray Shielding Test

To evaluate the gamma-ray shielding efficiency of the coatings, a Cs-137 gamma-ray source was selected due to its stable, low-energy emissions and long half-life, making it suitable for long-term shielding assessments. Testing was conducted under narrow-beam conditions, as shown in Figure 5 [37].

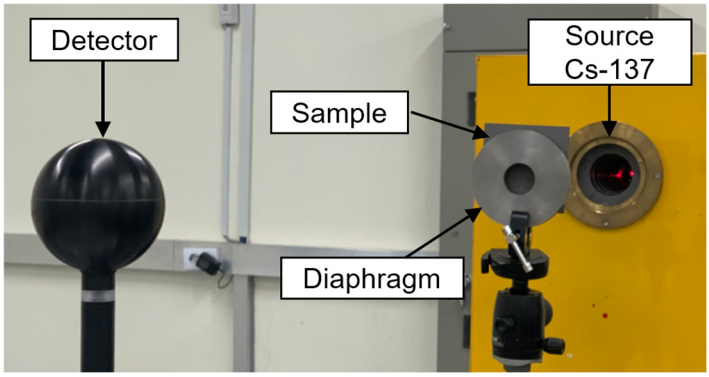


Figure 5. Experiment setup of the narrow beam geometry for evaluating the gamma-ray shielding performance of the coating.

The specimen was positioned such that the distance to the detector was at least ten times the detector diameter to minimize scattering effects, with a minimum clearance of 700 mm from the walls or the floor. Initially, the gamma-ray intensity (I_0) was measured without the specimen to establish a baseline reading. The specimen was then placed in the beam path and aligned with the diaphragm, and the transmitted intensity (I) was measured. Finally, the gamma-ray shielding efficiency was calculated using the following equation:

$$Shielding\ Efficiency(\%) = 1 - \frac{I}{I_0}$$

where I_0 represents the initial gamma-ray intensity, and I represents the intensity after passing through the specimen. This calculation enabled a direct comparison of gamma-ray shielding performance across coatings with varying WC contents.

3. Results and Discussion

3.1. Microstructural Characteristics

The morphology of coatings was characterized using a scanning electron microscope and an image analyzer. As shown in Table 3 and Figure 6, the coatings sprayed using the HVOF method exhibited a low porosity of less than 1% and a high density, regardless of the WC content in the coating materials. A typical microstructure generally observed in HVOF coatings was noted [38,39], and the thickness was close to the target of 250 µm. The microstructures of all coatings appeared to be non-uniform, with a mixture of white spots and gray spots of various shapes and sizes (a few microns) observed. In addition, no defects were observed at the interface between the coating and the substrate, indicating that all coatings demonstrated good adhesion to the substrate.

Table 3. Porosity and thickness of coatings with varying WC content.

Sample	Porosity (%)	Average Thickness (µm)
WC-85	<1	253
WC-73	<1	245
WC-66	<1	256
WC-39	<1	244

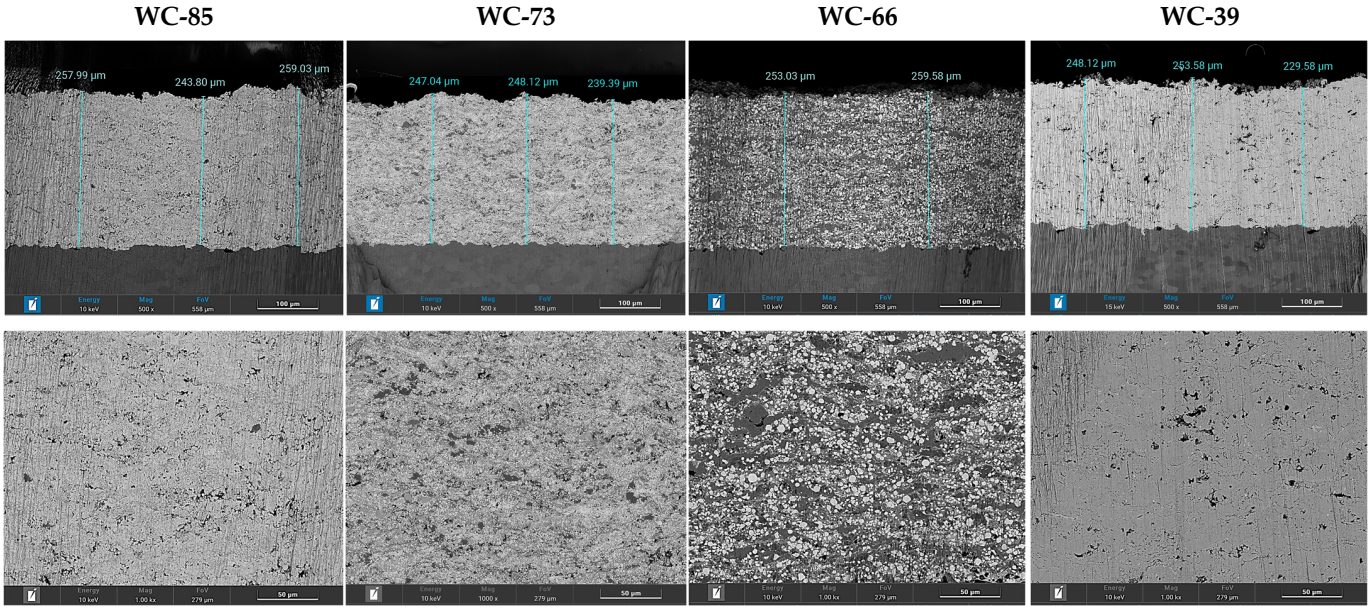


Figure 6. Cross-sectional SEM images of coatings with varying WC content.

Figure 7 presents high-magnification SEM images and EDS point and mapping analyses of the cross-sectional microstructure of the coatings, with detailed chemical compositions summarized in Table 4. Combining the results of EDS analysis with SEM image observations, it is evident that the bright particles in each image correspond to WC particles, while the relatively dark areas indicate the NiCr binder. The WC particles within the coating layer were distributed in proportion to the WC content, as confirmed by the EDS analysis, with the NiCr binder forming a matrix surrounding the WC particles. The coating layers of WC-85 and WC-73, primarily fabricated using 20 µm sized powder particles, exhibited a uniform distribution of WC particles effectively embedded within the NiCr binder matrix.

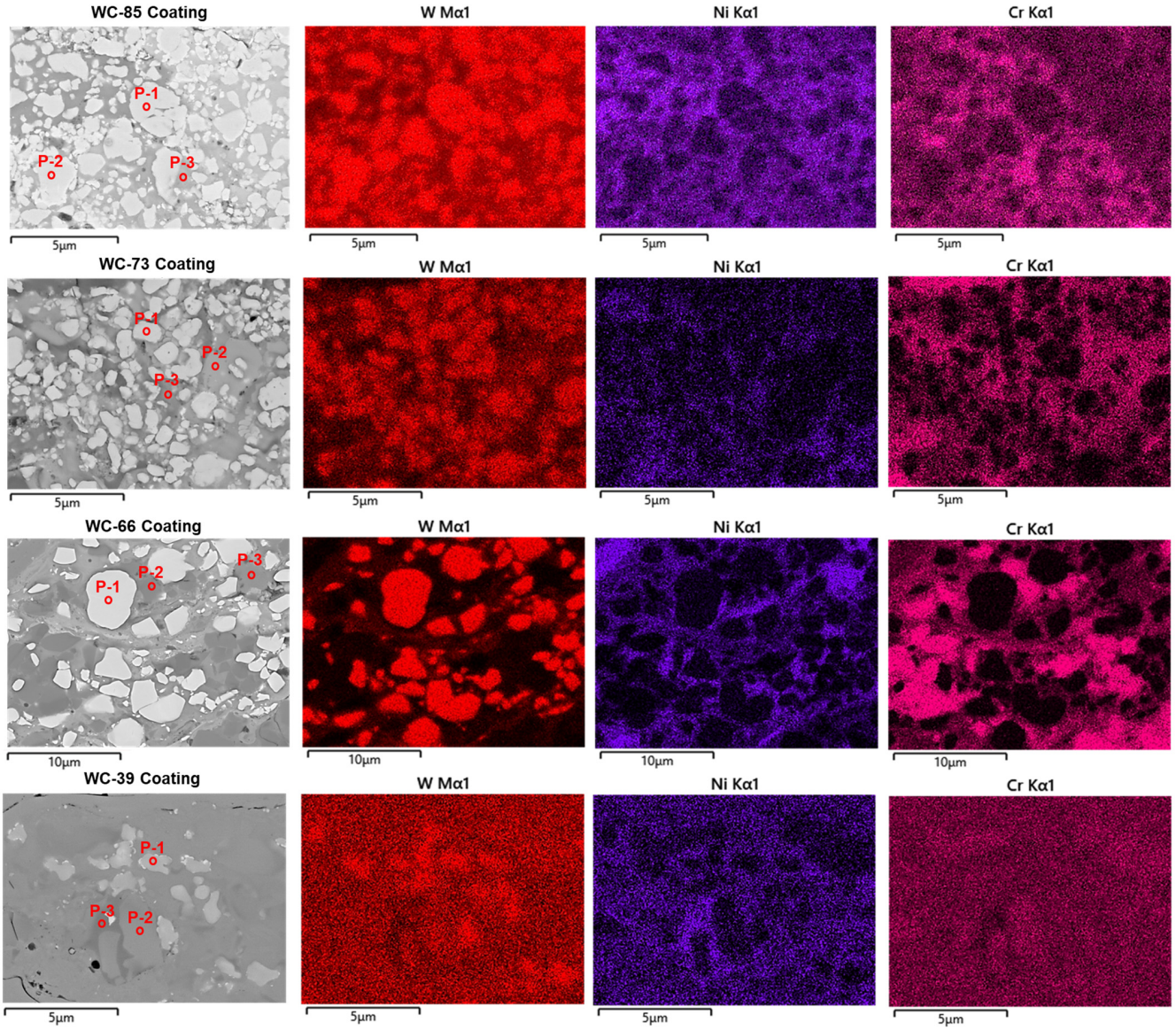


Figure 7. High-magnification cross-sectional SEM images of coatings with varying WC contents.

Table 4. Chemical composition of WC-NiCr coatings obtained from SEM-EDS point analysis at the locations indicated by red circles in Figure 7.

Sample	EDS Point	Chemical Composition (wt.%)			
		W	C	Ni	Cr
WC-85	P-1	90.6	8.1	1.3	-
	P-2	89.3	8.3	2.0	0.4
	P-3	34.5	1.8	49.9	13.8
WC-73	P-1	89.0	9.4	0.9	0.7
	P-2	58.1	9.5	31.6	0.8
	P-3	38.8	9.3	21.5	30.4
WC-66	P-1	91.1	8.9	-	-
	P-2	11.9	9.7	1.2	77.2
	P-3	3.4	4.8	72.3	19.5
WC-39	P-1	41.1	6.8	17.6	34.5
	P-2	35.7	7.6	9.4	47.3
	P-3	35.2	8.1	11.1	45.6

In contrast, WC-66 showed relatively large WC particles, attributed to the use of a mixture of powders smaller than 20 μm and larger than 45 μm. Cr-rich and Ni-rich phases were also observed in certain areas, likely resulting from chemical interactions between the binder and WC particles [40]. WC-39, having the lowest WC content, displayed a significantly reduced WC particle density within the coating layer. This coating exhibited the highest Cr content and lower Ni levels in the NiCr binder, reflecting the powder's composition. The reduced WC content in WC-39 is expected to result in comparatively lower wear resistance.

To investigate the effect of the HVOF process on changes in the chemical composition of the coating, EDS mapping was performed over a wide area of the coating cross-section to compare the chemical composition of the powder before spraying with that of the coating after spraying. The results are shown in Figure 8, and changes in chemical composition after the HVOF process are summarized in Table 5. For the four types of powders used in this study, no significant changes in chemical composition were observed after HVOF coating. When examining the representative elements, W, C, Ni, and Cr, there were slight increases or decreases in the coating after the HVOF process. However, the overall chemical composition did not differ greatly from that of the original powders.

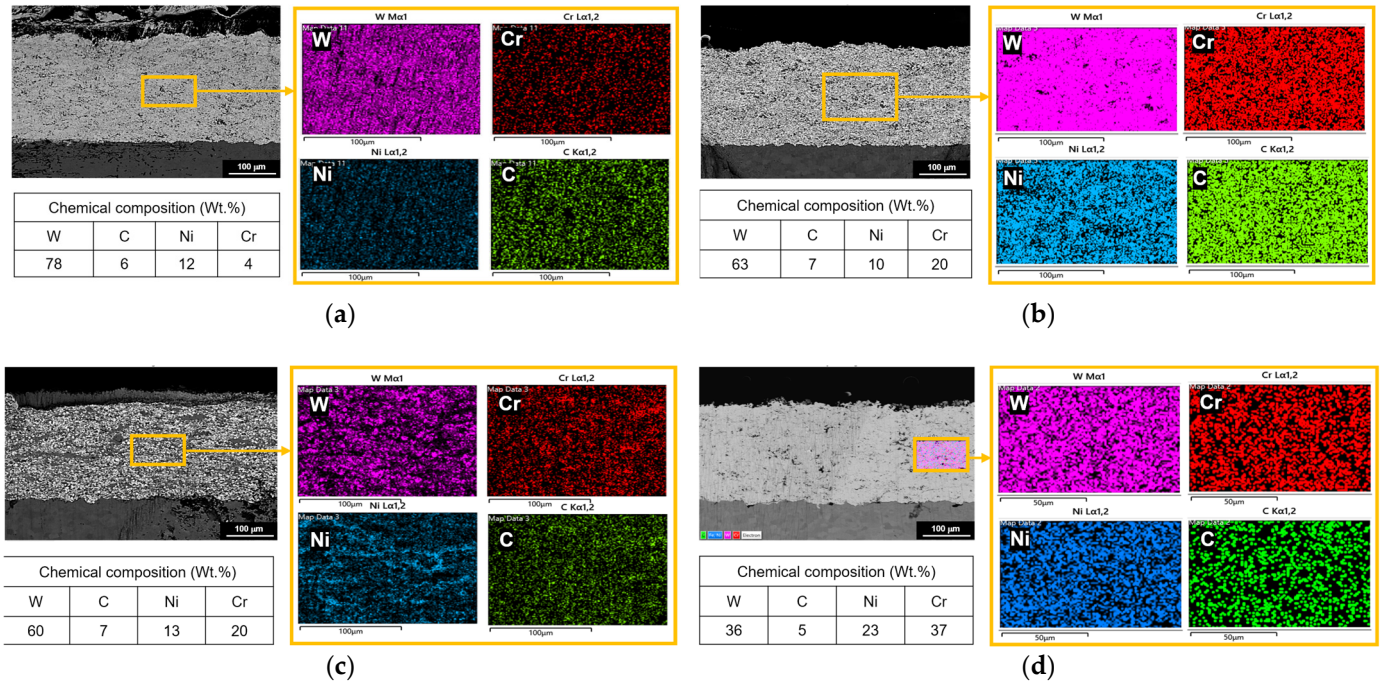


Figure 8. EDS mapping results of coatings with varying WC content: (**a**) WC-85, (**b**) WC-73, (**c**) WC-66, and (**d**) WC-39.

Table 5. Chemical composition change in coatings compared to starting powders (refer to Table 3).

Sample	Composition Change (wt. %)			
	W	C	Ni	Cr
WC-85	−1.2	+0.6	+1.8	−1.2
WC-73	−3.7	+1.1	+0.2	+0.1
WC-66	+0.5	+0.6	−3.3	−2.3
WC-39	+0.7	+1.4	+4.9	−6.0

It should be noted that EDS is a semi-quantitative technique and provides only approximate values for chemical composition due to limitations in detecting light elements and variations in sample preparation. Therefore, while the results presented in Table 4

indicate trends in chemical composition changes, they should not be interpreted as absolute values. Previous studies have reported that larger carbide particles are more likely to rebound during the spraying process, leading to an increased metallic binder content in the sprayed coating [19]. In this study, selecting an appropriate particle size suitable for HVOF minimized changes in chemical composition due to the spraying process. This ensured that the coatings retained compositions similar to the original powders, confirming the suitability of the selected process parameters.

3.2. Mechanical Properties and Corrosion Resistance

To investigate the effect of WC content in coatings on mechanical properties, Vickers hardness tests were conducted. Figure 9 shows the Vickers hardness indentation marks for coatings with varying WC content, and the hardness measurement results are presented in Figure 10. All coatings exhibited significantly higher hardness compared to the substrate material of the storage container, which measured 113.2 HV0.3. The coatings showed hardness values of 1091 HV0.3 for WC-85, 1083 HV0.3 for WC-73, 883 HV0.3 for WC-66, and 878 HV0.3 for WC-39. Furthermore, the hardness tended to increase with higher WC content in the coating. In general, WC possesses much higher hardness than the metal matrix, so an increase in WC content can lead to an improvement in hardness [41].

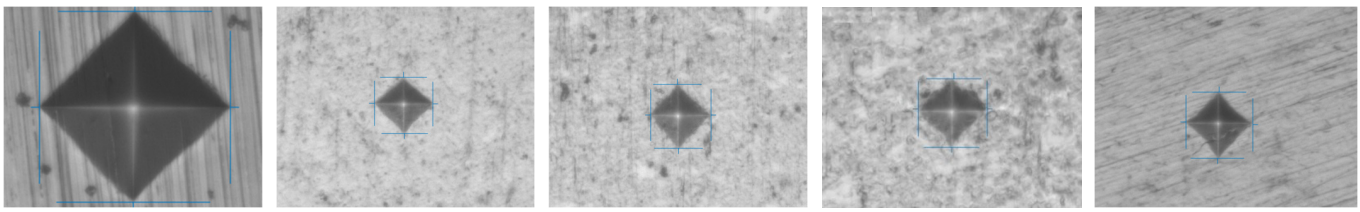


Figure 9. Vickers hardness indentation marks on coatings with varying WC content (500× magnification): (**a**) substrate material, (**b**) WC-85, (**c**) WC-73, (**d**) WC-66, and (**e**) WC-39.

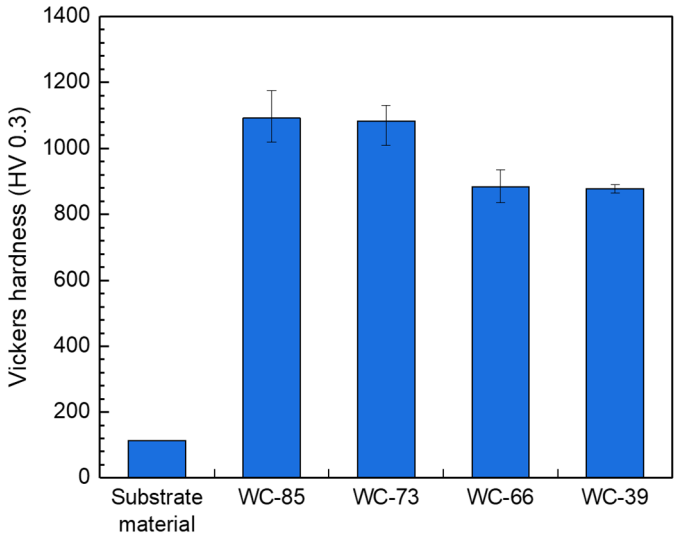


Figure 10. Vickers hardness of coatings with varying WC content.

Figure 11 shows the thickness reduction after 30,000 cycles of the Taber wear test for coatings with varying WC content and the substrate material. All coatings demonstrated significantly superior wear resistance compared to the substrate material. The average thickness reduction in the substrate was measured at 620 µm, while the coatings exhibited thickness reductions of 29 µm for WC-85, 32 µm for WC-73, 31 µm for WC-66, and 65 µm

for WC-39. Wear resistance tended to improve with increasing WC content, indicating a close relationship between hardness and wear resistance.

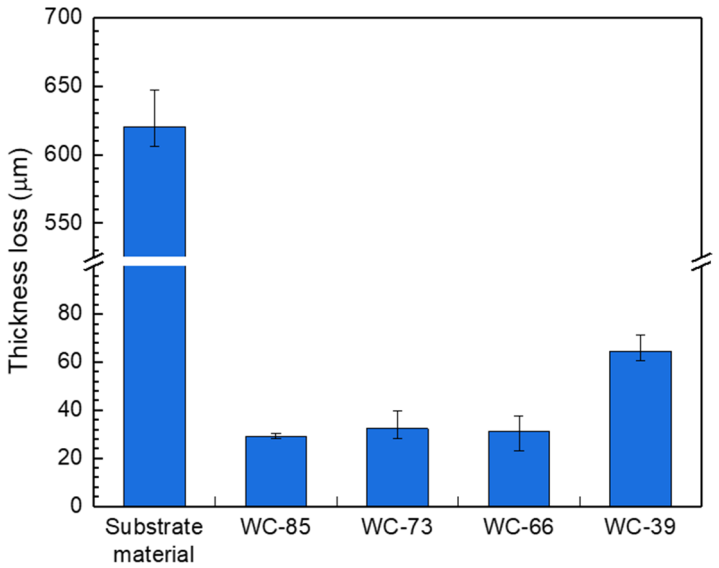


Figure 11. Comparison of relative wear resistance of coatings with varying WC content and the substrate material.

In general, hardness is one of the key mechanical properties influencing wear behavior and is widely used as a criterion for evaluating abrasive wear resistance [42]. Although the abrasive wear resistance of most metals is known to increase linearly with hardness, some materials do not show a consistent relationship between hardness and wear resistance [43,44]. For thermal spray coatings, increased hardness has also been reported to enhance wear resistance, primarily under dry wear conditions [45]. The coating materials used in this study similarly suggest that increased hardness under dry wear conditions can lead to improved wear resistance.

The adhesion strength measurements of the coatings with varying WC content are shown in Figure 12. The coatings exhibited average adhesion strengths of 82.2 MPa for WC-85, 65.2 MPa for WC-73, 77.4 MPa for WC-66, and 72 MPa for WC-39. Compared to other coating processes, such as cold spray, air plasma spray, and flame spray, the HVOF process is generally known for producing coatings with superior adhesion strength, typically in the range of 70–90 MPa [46]. In this study, all coatings except for WC-73 achieved adhesion strengths between 72 and 82 MPa, which can be considered excellent adhesion performance.

Electrochemical potentiodynamic polarization tests were performed at least twice for each coating with varying WC contents, and representative results are shown in Figure 13. For comparative purposes, the polarization curve of the substrate material is also presented to evaluate the corrosion resistance improvement. The corrosion parameters calculated via the Tafel extrapolation are summarized in Table 6.

Table 6. Electrochemical corrosion parameters of coatings with varying WC contents and the substrate material obtained from the cathodic Tafel extrapolation.

Sample	E_{corr} (V_{SCE})	i_{corr} ($\mu A/cm^2$)
Substrate material	−0.219	2.224
WC-85	−0.095	0.620
WC-73	−0.147	0.433
WC-66	−0.136	0.392
WC-39	−0.255	0.232

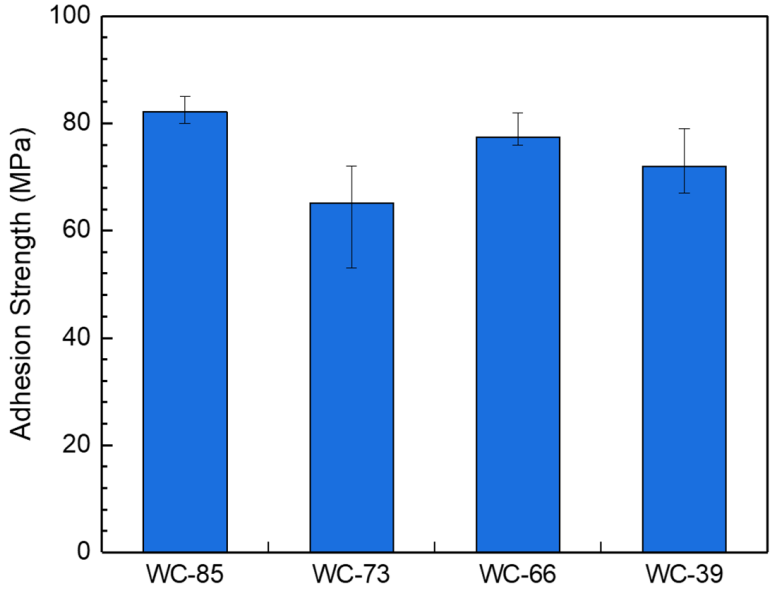


Figure 12. Adhesion strength of coatings with varying WC content.

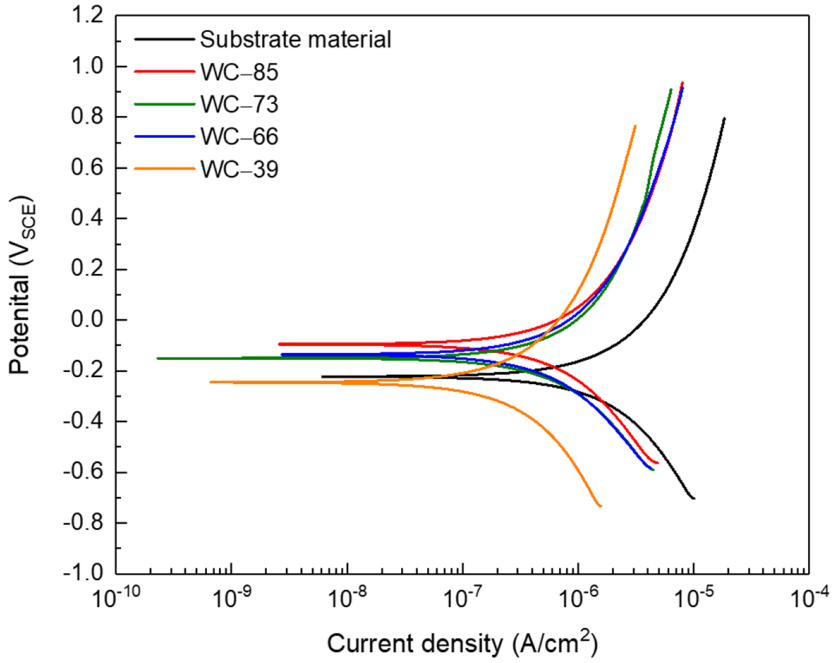


Figure 13. Potentiodynamic polarization curves of coatings with varying WC contents and the substrate material in the test solutions at 25 °C.

The WC-based coatings exhibited superior corrosion resistance compared to the substrate material. For the substrate, the corrosion current density was approximately 2.224 μA/cm^2, whereas significantly lower values were observed for the coatings: 0.620 μA/cm^2 for WC-85 (5.2 wt.% Cr), 0.433 μA/cm^2 for WC-73 (19.9 wt.% Cr), 0.392 μA/cm^2 for WC-66 (17.7 wt.% Cr), and 0.232 μA/cm^2 for WC-39 (43.0 wt.% Cr). These results indicate that the HVOF-applied WC-based coatings markedly enhance the corrosion resistance of the storage container substrate.

To determine the optimal Cr content for enhanced corrosion resistance, the corrosion current density was analyzed as a function of Cr content in the coatings, as shown in Figure 14. Chromium (Cr) is a well-established alloying element that improves corrosion resistance across a wide pH range, except in highly acidic or highly alkaline environments.

A Cr content of at least 10 wt.% is generally required to initiate passivation and significantly reduce the corrosion rate, with higher levels providing additional protection [47,48].

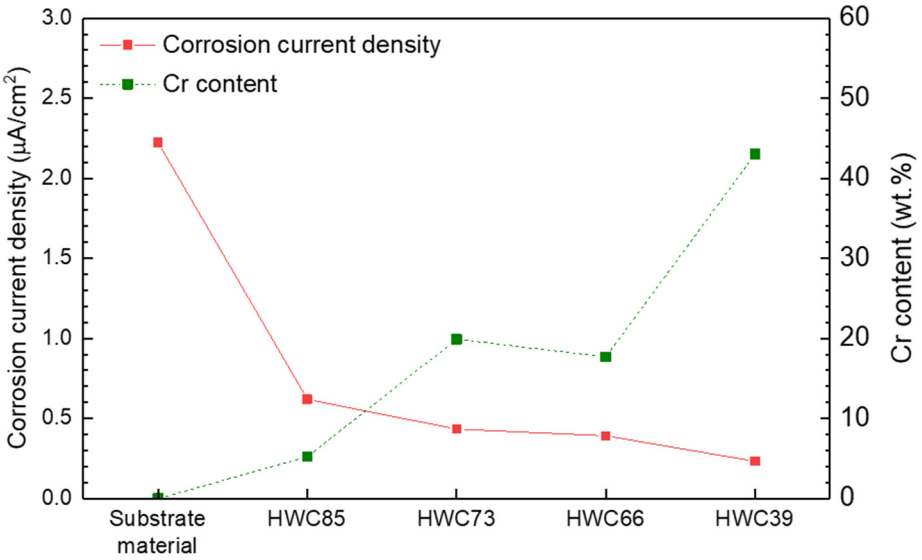


Figure 14. The relationship between Cr content in coating materials and corrosion current density.

As the Cr content in the coatings increased, corrosion current density decreased significantly, with WC-39 (43.0 wt.% Cr) exhibiting nearly half the value observed for WC-66 (17.7 wt.% Cr). These results suggest that while 17 wt.% Cr may offer adequate resistance under typical storage conditions, higher Cr contents provide superior corrosion resistance.

It should be noted that this study was conducted under aqueous conditions, while the actual storage environment is atmospheric. Atmospheric corrosion is highly dependent on relative humidity, with corrosion rates significantly decreasing when humidity levels fall below 60% [49–51]. Considering that typical LILW storage environments are maintained in controlled atmospheric conditions with relative humidity below this threshold, the WC-based coatings evaluated in this study are expected to exhibit even lower corrosion rates in practical applications.

Given that LILW storage environments are typically atmospheric and not highly corrosive, all coatings evaluated in this study are considered suitable for corrosion resistance. However, the results clearly demonstrate that coatings with higher Cr contents, such as WC-39, exhibit superior long-term durability and structural integrity under atmospheric conditions. These findings confirm that tailoring Cr content in WC-based coatings not only enhances corrosion resistance, but also ensures their effective application in scenarios demanding prolonged safety and reliability. Such coatings offer a robust solution for the safe management of radioactive waste, supporting the extended service life of storage containers under typical atmospheric conditions.

3.3. Gamma-Ray Shielding Performance

To evaluate the effectiveness of the coatings in enhancing gamma-ray shielding, the shielding efficiencies of an uncoated substrate and coatings with varying WC content were measured, as shown in Figure 15. The results clearly demonstrated that all coatings exhibited significantly higher shielding efficiency compared to the substrate alone. The substrate material achieved a shielding efficiency of 6.65%, whereas the coatings achieved 9.57% for WC-85, 8.98% for WC-73, 8.83% for WC-66, and 8.78% for WC-39.

Notably, the shielding performance improved with increasing WC content in the coatings. Tungsten (W), a primary component of WC, is well known for its effectiveness

in gamma-ray shielding due to its high atomic number and density. As supported by data presented in Table 7, materials with higher W contents tend to have lower half-value layer (HVL) values, indicating superior shielding capability [28]. Therefore, the excellent shielding performance of WC-85 can be attributed to its high W content, which enhances its ability to attenuate gamma radiation.

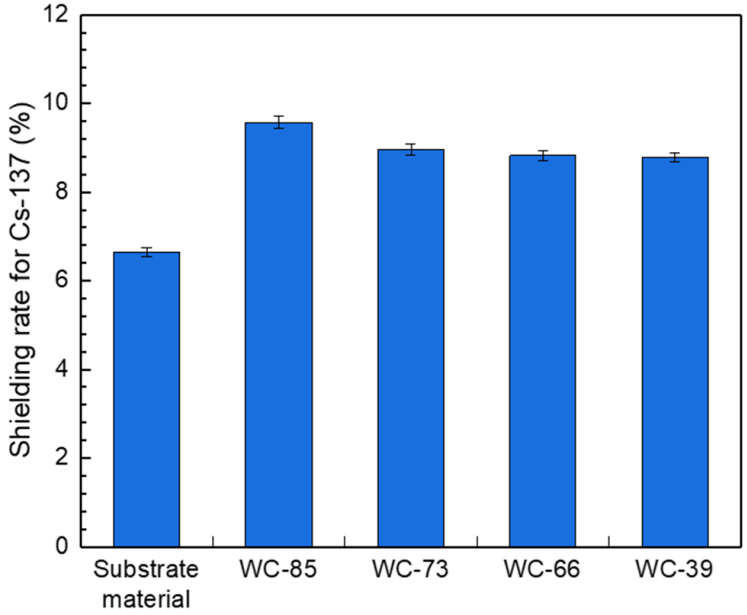


Figure 15. Comparison of gamma-ray shielding efficiency between coatings with varying WC content and the substrate material.

Table 7. Density and half value layer (HVL) of various metallic materials.

Element	Density (g/cm^3)	HVL * for Co-60 (cm)
W	19.30	0.8
Pb	11.34	1.2
Bi	9.80	1.4
Cu	8.96	1.9
Fe	7.86	2.2
Al	2.70	6.8

* The thickness of a material required to reduce the intensity of radiation by half (50%).

However, these results reflect not only the material properties of the coatings, but also the added thickness contributed by the coating layer, as the coated samples are inherently thicker than the uncoated substrate. To independently evaluate the intrinsic shielding performance of the coatings, additional experiments were conducted using WC-85 coatings with varying thicknesses while maintaining a fixed substrate thickness of 1.2 mm. WC-85 was selected for these experiments due to its superior performance demonstrated in Figure 15. This approach eliminates the confounding factor of thickness differences and isolates the contribution of the coating itself.

As shown in Figure 16, cross-sectional SEM images were used to confirm the thickness and uniformity of the WC-85 coatings. The total thickness, including the 1.2 mm substrate, was measured as 1.45 mm, 1.55 mm, 1.65 mm, and 1.75 mm for coatings with nominal thicknesses of 250 µm, 350 µm, 450 µm, and 550 µm, respectively. The SEM images revealed dense and defect-free coatings produced by the HVOF process, providing a reliable basis for further evaluation of the coating's shielding performance.

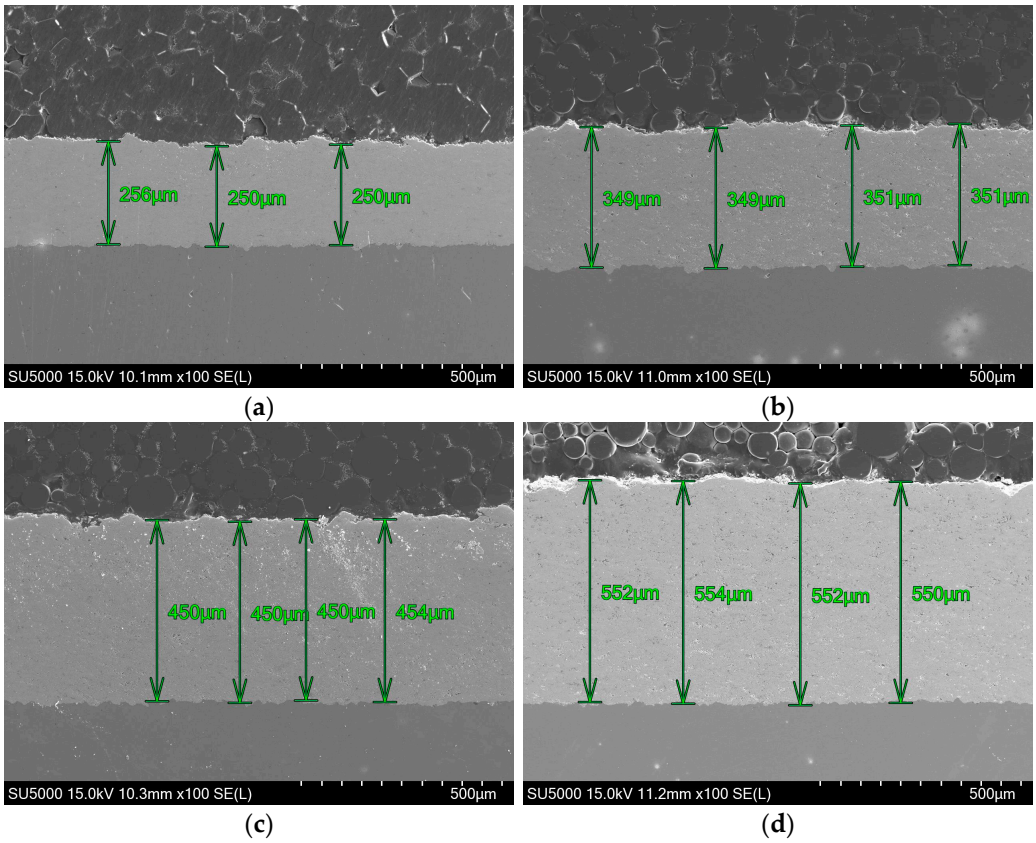


Figure 16. Cross-sectional SEM images of WC-85 coatings with varying thicknesses: (**a**) 250 µm, (**b**) 350 µm, (**c**) 450 µm, and (**d**) 550 µm.

To directly compare the gamma-ray shielding efficiency of WC-85 coatings to that of the uncoated substrate, shielding efficiencies were plotted as a function of total thickness, as shown in Figure 17. Linear regression analysis demonstrated a strong linear relationship for both the coated and uncoated samples, with R^2 values of 0.9952 and 0.9991, respectively. At the same total thickness, the WC-85 coating consistently surpassed the uncoated substrate, clearly demonstrating the superior shielding performance of the WC-based coating itself. In addition, the gamma-ray shielding efficiency of the WC-85 coating increased more significantly with total thickness compared to the uncoated substrate. This is evidenced by the more significant slope of the linear regression for the WC-85-coated samples. The higher slope indicates that as the thickness of the WC coating increases, and consequently, the fraction of WC in the total thickness becomes greater, the shielding efficiency improves at a faster rate. This behavior highlights the exceptional gamma-ray attenuation properties of WC, further supporting its effectiveness as a shielding material. These results confirm that the intrinsic material properties of WC-85 contribute significantly to its gamma-ray shielding efficiency, independent of the added thickness.

In summary, the combined analysis of Figures 15–17 validates the effectiveness of WC-based coatings in significantly enhancing gamma-ray shielding. By isolating the coating's contribution, it is evident that WC-85 offers superior shielding performance, making it an ideal material for improving the safety and durability of storage containers for LILWs.

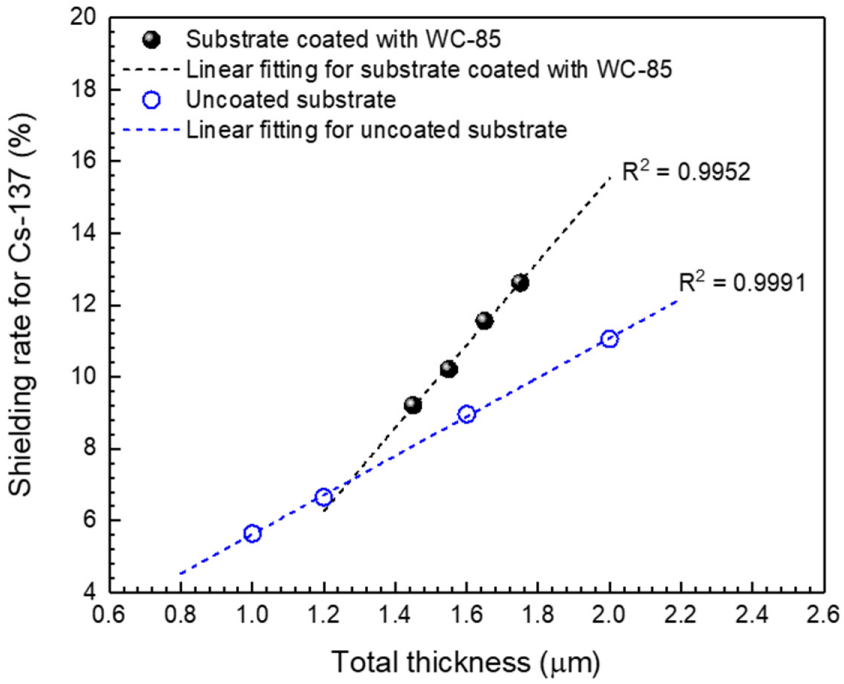


Figure 17. Gamma-ray shielding efficiency for Cs-137 as a function of total thickness for WC-85-coated and uncoated substrates.

4. Conclusions

To enhance the durability and performance of storage containers for LILWs, coatings with varying WC contents were applied using the HVOF method and subjected to comprehensive property evaluations. The key findings from the analysis of mechanical properties, corrosion resistance, and gamma-ray shielding performance are summarized as follows:

- The coatings exhibited significantly higher hardness compared to the substrate material, with hardness increasing proportionally to the WC content.
- Higher WC content in the coatings resulted in enhanced wear resistance, directly attributed to the increased hardness.
- Adhesion strength was consistent across all WC contents, with most coatings demonstrating excellent adhesive properties, exceeding approximately 70 MPa, except for WC-73.
- Corrosion resistance improved with higher Cr content in the coatings. WC-39, with the highest NiCr content, exhibited superior performance in this regard.
- Gamma-ray shielding performance was significantly enhanced with increased W content due to its high atomic number. The WC-85 coating, which contained the highest W content, demonstrated over a 40% improvement in shielding efficiency compared to the uncoated substrate of the same thickness.
- Depending on the storage container's operational environment and durability requirements, the composition of NiCr and WC in coatings can be tailored to optimize specific properties such as corrosion resistance, mechanical strength, or gamma-ray shielding efficiency.

These results confirm that WC-based coatings applied via the HVOF method are promising candidates for enhancing the durability and radiation shielding capabilities of LILW storage containers.

Author Contributions: Conceptualization and writing—review and editing, G.D.S. and S.H.B.; methodology, formal analysis, and investigation, Y.-H.S., B.K.K., J.H.H. and J.H.L.; writing—original draft preparation, Y.-H.S. All authors have read and agreed to the published version of the manuscript.

Funding: This research was supported by the Technology Development Program (S3324582) funded by the Ministry of SMEs and Startups (MMS, Republic of Korea). Additional support was provided by the National Research Foundation of Korea (NRF) grant funded by the Korean government (Ministry of Science and ICT) (No. 2022M2D4A1054827).

Data Availability Statement: The data supporting the findings of this study are available from the corresponding author upon reasonable request. However, access to the data is restricted due to privacy and ethical considerations.

Conflicts of Interest: Authors Yeong-Ho Son, Seung Heon Baek, Beom Kyu Kim, Jeong Ho Hwang, Jae Hun Lee and Geun Dong Song were employed by the company FNC Technology Co., Ltd. The authors declare that the research was conducted in the absence of any commercial or financial relationships that could be construed as a potential conflict of interest.

References

1. IAEA. *Long Term Behaviour of Low and Intermediate Level Waste Packages Under Repository Conditions*; IAEA-TECHDOC-1397; IAEA: Vienna, Austria, 2004.
2. Byeon, H.; Jeong, G.Y.; Park, J. Structural stability analysis of waste packages containing low- and intermediate-level radioactive waste in a silo-type repository. *Nucl. Eng. Technol.* **2021**, *53*, 1524–1533. [CrossRef]
3. Ahn, J.; Kim, W.S.; Park, J.B.; Francis, A.J.; Um, W. Temporal changes of geochemistry and microbial community in low and intermediate level waste (LILW) repository, South Korea. *Ann. Nucl. Energy* **2019**, *128*, 309–317. [CrossRef]
4. IAEA. *Containers for Packaging of Solid and Intermediate Level Radioactive Wastes*; Technical Reports Series NO. 355; IAEA: Vienna, Austria, 1993.
5. Vehovar, L.; Tandler, M. Stainless steel containers for the storage of low and medium level radioactive waste. *Nucl. Eng. Des.* **2001**, *206*, 21–33. [CrossRef]
6. Bonin, H.W.; Walker, M.W.; Bui, V.T. Application of Polymers for the Long-Term Storage and Disposal of Low- and Intermediate-Level Radioactive Waste. *Nucl. Technol.* **2004**, *145*, 82–101. [CrossRef]
7. Uhm, Y.R.; Kim, J.; Jung, J.; Rhee, C.K. Fabrications of pva coated nano-b_4c reinforced hdpe composites. *Mod. Phys. Lett. B* **2009**, *23*, 3931–3936. [CrossRef]
8. Jung, J.; Kim, J.; Uhm, Y.R.; Jeon, J.K.; Lee, S.; Lee, H.M.; Rhee, C.K. Preparations and thermal properties of micro- and nano-BN dispersed HDPE composites. *Thermochim. Acta* **2010**, *449*, 8–14. [CrossRef]
9. Ghattas, N.K.; Eskander, S.B.; Bayoumi, T.A.; Saleh, H.M. Cement-Polymer Composite Containers for Radioactive Wastes Disposal. *J. Radiat. Res. Appl. Sci.* **2009**, *2*, 103–118.
10. Nie, H.; Li, Z.; Zhou, H.; Wu, J.; Wen, G.; Li, Y. Study on the wear resistance and mechanism of HVOF-sprayed WC10Co4Cr coatings. *Surf. Coat. Technol.* **2024**, *494*, 131368. [CrossRef]
11. Kumar, V.; Verma, R. Effect of GNP and laser-surface texturing on HVOF sprayed WC10Co4Cr coatings for high-wear resistance. *Tribol. Int.* **2023**, *178*, 108057. [CrossRef]
12. Kumar, R.; Sharma, S.; Singh, J.P.; Gulati, P.; Singh, G.; Dwivedi, S.P.; Li, C.; Kumar, A.; Tag-Eldin, E.M.; Abbas, M. Enhancement in wear-resistance of 30MNCRB5 boron steel-substrate using HVOF thermal sprayed WC–10% Co–4% Cr coatings: A comprehensive research on microstructural, tribological, and morphological analysis. *J. Mater. Res. Technol.* **2023**, *27*, 1072–1096. [CrossRef]
13. Mishra, B.B.; Nautiyal, H. Frictional and wear behavior of Cr_3C_2-NiCr coating on AISI-304 stainless steel. *Adv. Mater. Process. Technol.* **2022**, *8*, 4007–4017. [CrossRef]
14. Wen, Y.; Zhang, Y.; Zhang, X.; Zhao, Z.; Yan, Q. The tribological behavior of Cu-based brake materials against Cr_3C_2-NiCr coated steel disks with varying roughness. *Tribol. Trans.* 2024; *accepted*.
15. Kumar, N.; Choubey, V.K. Experimental investigation on hot corrosion, oxidation and microstructure of WC based cermet HVOF coating. *High Temp. Corros. Mater.* **2024**, *101*, 413–432. [CrossRef]
16. Pereira, P.; Rocha, A.F.; Sacramento, J.; Oliveira, F.J.; Senos, A.M.R.; Malheiros, L.F.; Bastos, A.C. Corrosion resistance of WC hardmetals with different Co and Ni-based binders. *Int. J. Refract. Met. Hard Mater.* **2022**, *104*, 105799. [CrossRef]
17. Wang, K.; Hong, S.; Wei, Z.; Hu, N.; Cheng, J.; Wu, Y. Long-term corrosion behavior of HVOF sprayed Cr_3C_2–NiCr coatings in sulfide-containing 3.5 wt.% NaCl solution. *J. Mater. Res. Technol.* **2021**, *15*, 3122–3132. [CrossRef]
18. Chen, X.; Wang, H.T.; Ji, G.C.; Bai, X.B.; Fu, W. Microstructure and properties of TiB2–Ni coatings with different binder phase 452 contents deposited by HVOF spray process. *Rare Met.* **2022**, *41*, 1385–1393. [CrossRef]

19. Li, C.J.; Ji, G.C.; Wang, Y.Y.; Sonoya, K. Dominant effect of carbide rebounding on the carbon loss during high velocity oxy-fuel 454 spraying of Cr_3C_2–NiCr. *Thin Solid Film.* **2002**, *419*, 137–143. [CrossRef]
20. Jose, S.A.; John, M.; Menezes, P.L. Cermet systems: Synthesis, properties, and applications. *Ceramics* **2022**, *5*, 210–236. [CrossRef]
21. Zhang, F.; Tabecki, A.; Bennett, M.; Begg, H.; Lionetti, S.; Paul, S. Feasibility Study of High-Velocity Oxy-fuel (HVOF) Sprayed Cermet and Alloy Coatings for Geothermal Applications. *J. Therm. Spray Technol.* **2023**, *32*, 339–351. [CrossRef]
22. Wielage, B.; Wank, A.; Pokhmurska, H.; Grund, T.; Rupprecht, C.; Reisel, G.; Friesen, E. Development and trends in HVOF spraying technology. *Surf. Coat. Technol.* **2006**, *201*, 2032–2037. [CrossRef]
23. Staia, M.H.; Mejias, A.; Kossman, S.; Puchi-Cabrera, E.S. Tribocorrosion Performance of WC-12Co HVOF-Sprayed Coatings Reinforced with Carbon Nanotubes. *Crystals* **2023**, *13*, 457. [CrossRef]
24. Berger, L.M.; Saaro, S.; Naumann, T.; Wiener, M.; Weihnacht, V.; Thiele, S.; Suchánek, J. Microstructure and properties of HVOF-sprayed chromium alloyed WC–Co and WC–Ni coatings. *Surf. Coat. Technol.* **2008**, *202*, 4417–4421. [CrossRef]
25. Song, B.; Murray, J.W.; Wellman, R.G.; Pala, Z.; Hussain, T. Dry sliding wear behaviour of HVOF thermal sprayed WC-Co-Cr and WC-Cr_xC_y-Ni coatings. *Wear* **2020**, *442*, 203114. [CrossRef]
26. Wu, Y.; Hong, S.; Zhang, J.; He, Z.; Guo, W.; Wang, Q. Microstructure and cavitation erosion behavior of WC–Co–Cr coating on 1Cr18Ni9Ti stainless steel by HVOF thermal spraying. *Int. J. Refract. Met. Hard Mater.* **2012**, *32*, 21–26. [CrossRef]
27. El Rayes, M.M.; Sherif, E.S.M.; Abdo, H.S. Comparative study into microstructural and mechanical characterization of HVOF-WC-based coatings. *Crystals* **2022**, *12*, 969. [CrossRef]
28. McAlister, D.R. *Gamma Ray Attenuation Properties of Common Shielding Materials*; University Lane Lisle: Lisle, IL, USA, 2012.
29. Thermal Spray Powder. Available online: https://www.alloymstech.com/Coating-Powder.php (accessed on 10 December 2024).
30. *ASTM E384*; Standard Test Method for Microindentation Hardness of Materials. ASTM International: West Conshohocken, PA, USA, 2005.
31. Song, G.D.; Hwang, J.H.; Kim, D.W.; Park, B.C.; Hahn, J.; Hong, S.G. Coexistence of two distinct fatigue failure mechanisms in Super304H welded joint at elevated temperatures. *Mater. Sci. Eng. A* **2021**, *819*, 141462. [CrossRef]
32. *ASTM F1978*; Standard Test Method for Measuring Abrasion Resistance of Metallic Thermal Spray Coatings by Using the Taber Abraser. ASTM International: West Conshohocken, PA, USA, 2001.
33. Wank, A.; Wielage, B.; Reisel, G.; Grund, T.; Friesen, E. Performance of thermal spray coatings under dry abrasive wear conditions. In Proceedings of the Coatings, Erlangen, Germany, 5–7 April 2004.
34. *ASTM C633*; Standard Test Method for Adhesion or Cohesion Strength of Thermal Spray Coatings. ASTM International: West Conshohocken, PA, USA, 2021.
35. Kim, J.H. Atmospheric acidic deposition: State of acid rain in Korea and the world. *Korean J. Ecol.* **2005**, *28*, 169–180. [CrossRef]
36. Song, G.D.; Jeon, S.H.; Son, Y.H.; Kim, J.G.; Hur, D.H. Galvanic effect of magnetite on the corrosion behavior of carbon steel in deaerated alkaline solutions under flowing conditions. *Corros. Sci.* **2018**, *131*, 71–80. [CrossRef]
37. Qadr, H.M. Calculation for gamma ray buildup factor for aluminium, graphite and lead. *Int. J. Nucl. Energy Sci. Technol.* **2019**, *13*, 61–69. [CrossRef]
38. Lamana, M.S.; Pukasiewicz, A.G.; Sampath, S. Influence of cobalt content and HVOF deposition process on the cavitation erosion resistance of WC-Co coatings. *Wear* **2018**, *398*, 209–219. [CrossRef]
39. Nahvi, S.M.; Jafari, M. Microstructural and mechanical properties of advanced HVOF-sprayed WC-based cermet coatings. *Surf. Coat. Technol.* **2016**, *286*, 95–102. [CrossRef]
40. Agüero, A.; Camón, F.; García de Blas, J.; Del Hoyo, J.C.; Muelas, R.; Santaballa, A.; Ulargui, S.; Vallés, P. HVOF-deposited WCCoCr as replacement for hard Cr in landing gear actuators. *J. Therm. Spray Technol.* **2011**, *20*, 1292–1309. [CrossRef]
41. Klaasen, H.; Kübarsepp, J. Abrasive wear performance of carbide composites. *Wear* **2006**, *261*, 520–526. [CrossRef]
42. Jeong, D.H.; Erb, U.; Aust, K.T.; Palumbo, G. The relationship between hardness and abrasive wear resistance of electrodeposited nanocrystalline Ni–P coatings. *Scr. Mater.* **2003**, *48*, 1067–1072. [CrossRef]
43. Hokkirigawa, K.; Kato, K.; Li, Z.Z. The effect of hardness on the transition of the abrasive wear mechanism of steels. *Wear* **1988**, *123*, 241–251. [CrossRef]
44. Khruschov, M.M. Principles of abrasive wear. *Wear* **1974**, *28*, 69–88. [CrossRef]
45. Houdková, Š.; Zahálka, F.; Kašparová, M.; Berger, L.M. Comparative study of thermally sprayed coatings under different types of wear conditions for hard chromium replacement. *Tribol. Lett.* **2011**, *43*, 139–154. [CrossRef]
46. Shinde, S.; Sampath, S. A critical analysis of the tensile adhesion test for thermally sprayed coatings. *J. Therm. Spray Technol.* **2022**, *31*, 2247–2279. [CrossRef]
47. Jones, D.A. *Principles and Prevention*, 2nd ed.; Prentice Hall: Upper Saddle River, NJ, USA, 1996.
48. *A Designers' Handbook Series, Design Guidelines for the Selection and Use of Stainless Steels*; Nickel Institute: Toronto, ON, Canada, 2020.
49. Xiang, Y.; Wang, Z.; Yang, X.; Li, Z.; Ni, W. The upper limit of moisture content for supercritical CO_2 pipeline transport. *J. Supercrit. Fluids* **2012**, *67*, 14–21. [CrossRef]

50. Folić, R.; Zenunović, D. Durability design of concrete structures, Part 2: Modelling and structural assessment. *Facta Univ. -Ser. Archit. Civ. Eng.* **2010**, *8*, 45–66. [CrossRef]
51. Bossio, A.; Bitondo, C.; Monetta, T.; Bellucci, F.; Mollo, L. Corrosion of steel arches in support of tuff masonry. A case study. In Proceedings of the EUROSTEEL 2014, Naples, Italy, 10–12 September 2014.

Disclaimer/Publisher's Note: The statements, opinions and data contained in all publications are solely those of the individual author(s) and contributor(s) and not of MDPI and/or the editor(s). MDPI and/or the editor(s) disclaim responsibility for any injury to people or property resulting from any ideas, methods, instructions or products referred to in the content.